Euler-Lagrange-Model-Based Torque Assignment Control for Dual In-Wheel PM Motors With Voltage Vectors Integrated Modulation

Zhaoheng Wang, Lei Xu, *Member, IEEE*, Xiaoyong Zhu, *Member, IEEE*, Li Quan, Wen-Hua Chen, *Fellow, IEEE*, Lizhang Xu, and Shihong Ding, *Senior Member, IEEE*

***Abstract*—In this article, an Euler-Lagrange-model based torque assignment (ELM-TA) control scheme is proposed for a distributed drive (DD) system with multiple in-wheel motors. It focuses on the torque assignment of the multiple motors in DD system, in order to achieve optimal dynamic performance, synchronization, and reliability. Considering the flexible coupling effects, an Euler-Lagrange model is formulated for 1/2 DD system with dual in-wheel permanent magnet (DIW-PM) motors. As a consequence of the nonlinear characteristic of the drive system with DIW-PM motors, direct torque control with multivoltage vector integrated modulation is implemented with the objective of enhancing the reliability and robustness of the drive system. In addition, the Euler-Lagrange-model based controller is designed for the motor control unit, where the dynamic tuning strategy of interconnection and friction damping coefficients is developed to achieve dynamic decoupling of state variables. Finally, the experimental setups are constructed by considering the different drive modes. The experimental results verify the validity and reliability of the proposed approach, which shows a good potential candidate for a distributed electric vehicle drive system.**

***Index Terms*—Direct torque control, distributed drive, Euler Lagrange model, integrated torque assignment, in-wheel permanent magnet motor.**

I. Introduction

DISTRIBUTED drive (DD) has recently exhibited the potential to become a significant component in electric traction systems, owing to its advantages including four-wheel independence traction and short transmission chains with high efficiency [1], [2], [3]. Yet, for the electric traction application, the goal is to achieve not only a single highly reliable and responsive motor drive, but also to ensure that the control between the multiple independent motor drive systems is synergistic and consistent. Hence, how to achieve the cooperative control of multiple traction motors has emerged as a pressing concern within the domain of distributed systems.

At present, in order to satisfy the stability, safety, and economy of DD system for EVs application, the motors of the DD system usually adopt hierarchical cooperative control [4], [5]. And, the control algorithm can be divided into cooperative control algorithm based on vehicle control unit (VCU) and motor control unit (MCU) [6].

On the one hand, to solve the problem of multiple motors control in DD system, the advanced control theories and methods are employed in VCU. In [7], with energy utilization efficiency and tire load as objectives, based on the motor driving capacity and tire adhesion limit, weight factors are used to coordinate and optimize the torque increment of each in-wheel motor, achieving cooperative driving of all actuators. In [8], three torque distribution strategies based on different road conditions are proposed, taking into account vehicle dynamic loads and road friction, to ensure lateral stability requirements and improve vehicle driving stability. Moreover, by using the optimal allocation (OA) algorithm, the optimal power consumption is taken as the objective function to solve a quadratic programming problem and achieve optimal torque allocation that effectively balances considerations of safety and economy [9]. Nonetheless, the upper-level controller is particularly vulnerable to the external factors, including operating conditions, road excitation and etc., which always give rise to nonlinearities in the DD traction system [10]. At present, many coordinated torque algorithms designed for the multiple motors drive primarily rely on linear models, neglecting the electromagnetic and mechanical coupling effects among in-wheel motors, which are often uniformly regarded as external disturbances. And, the process of

Received 6 October 2024; revised 14 January 2025 and 1 March 2025; accepted 14 March 2025. This work was supported in part by the Key International (Regional) Cooperative Research Programs of National Natural Science Foundation of China under Grant 52320105009 and in part by the Joint Key Project of National Natural Science Foundation of China under Grant U24A20146. *(Corresponding author: Lei Xu.)*

Zhaoheng Wang, Lei Xu, Xiaoyong Zhu, Li Quan, and Shihong Ding are with the School of Electrical and Information Engineering, Jiangsu University, Zhenjiang 212013, China (e-mail: 2222207035@stmail.ujs.edu.cn; leixu@ujs.edu.cn; zxyff@ujs.edu.cn; quanli@ujs.edu.cn; dsh@ujs.edu.cn).

Wen-Hua Chen is with the Department of Aeronautical and Automotive Engineering, Loughborough University, LE11 3TU Loughborough, U.K. (e-mail: w.chen@lboro.ac.uk).

Lizhang Xu is with the School of Agricultural Engineering, Jiangsu University, Zhenjiang 212013, China (e-mail: justxlz@ujs.edu.cn).

Digital Object Identifier 10.1109/TIE.2025.3555041

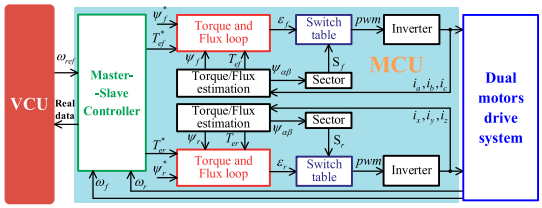

Fig. 1. Master-Slave control for DIW-PM motors drive system.

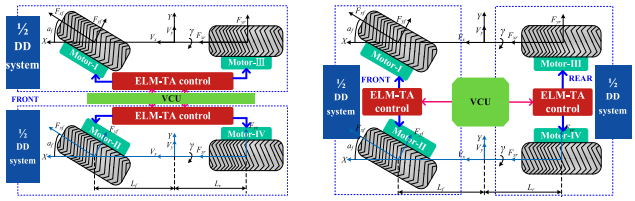

Fig. 2. Block diagram of the DIW-PM motors drive system. (a) FR in-wheel drive mode. (b) LR in-wheel drive mode.

linearization during the initial phase may result in the omission of certain nonlinear components, and this uncertainty modeling will lead to speed instability and torque mismatch in distributed traction system [11].

Therefore, in order to obtain more realistic descriptions of vehicle models, neural network [12], Euler-Lagrange (EL) model [13], and D'Alembert description [14] are often employed to achieve data modeling. In [15], a novel modelling method based on the recurrent high-order neural network is proposed for the lateral steady-state performance of in-wheel motor driven vehicles. Besides, an adaptive Lagrange discretization method is proposed in [16], which fits the nonlinear vehicle dynamics function.

On the other hand, the MCU is employed as the cooperative controller, receiving directives from the VCU, coordinating the driving voltage or current of each motor, and facilitating cooperative control among multiple controllers and actuators in MCU. As shown in Fig. 1, generally, the typical master-slave control in MCU for two motors drive system is proposed in [17], [18], [19]. And the direct torque control is employed to achieve torque assignment control. In [20], the allocation of q-axis current is determined by the dynamic coordination coefficient, which serves to enhance the steering response of the dual motor system and facilitate rapid path tracking during vehicle turning and driving maneuvers. Meanwhile, according to the estimation of tracking path and movement distance by the inertial measurement unit sensor, a compensatory mechanism is proposed in [21] to provide feedback compensation and modify the dual motor commands, thereby enhancing the accuracy of the vehicle tracking performance.

However, the multiple motors and controllers are widely used in the bottom architecture of DD systems, which leads to communication interference among these components. The presence of redundant structures further elevates the risk of potential failures, thereby presenting a significant challenge to the robustness of VCU [22], [23]. Consequently, there are still a number of challenges to be overcome in order to achieve cooperative control of multiple motors within the distributed drive system.

In order to address the aforementioned issues, a torque assignment control method based on the Euler-Lagrange model (ELM) is proposed in this article. The main contributions of this article are summarized as follows.

1) The flexible coupling effect in a 1/2 DD system with dual in-wheel permanent magnet (DIW-PM) motors is analyzed in detailed. On this basis, by adopting the Euler-Lagrange-model, the mathematic model of the DD system is deduced and established.
2) Based on the direct torque control with multivoltage vector integrated modulation, the Euler-Lagrange model based torque assignment (ELM-TA) control is presented. And, the Euler-Lagrange Controller is designed to realize the torque assignment of the DD system.
3) Considering the influence mechanism coupling between each in-wheel motor, the dynamic parameters tuning is proposed where the robustness of the DD system with DIW-PM motors is enhanced.

The rest of this article is structured as follows. The mathematical model is established based on the EL formula, whereby the electrical and mechanical balance equations of the mechatronic system are combined in Section II. In Section III, based on the integrated direct torque control theory, a torque assignment control with multivoltage vectors (MVV) integrated modulation is investigated in detail. Section IV presents a series of experiments conducted under a variety of typical road conditions, with a comparison drawn between the results and those obtained using the traditional master-slave control method. Finally, the conclusions and future directions will be drawn in Section V.

II. Modeling of the DIW-PM Motors Drive System

For the traditional four-wheel independent DD system, it is necessary to utilize four MCUs, four drive motors and a VCU as the basic structural components. In order to reduce the number of MCUs and enhance the system's robustness and responsiveness, an integrated control concept is employed that utilizes a single MCU for the management of multiple drive motors. Nevertheless, the four in-wheel PM motors drive the four wheels, where the front and rare (FR) in-wheel drive system or left and right (LR) in-wheel drive systems are all spatially symmetrical. Moreover, in order to simplify the modeling, as shown in Fig. 2, the 1/2 DD system with in-wheel PM motors is selected as the control example.

Therefore, based on the principles of the EL model, the DIW-PM drive system is modeled, considering various factors associated with motors and mechanical components. Subsequently, the mathematical model of the DIW-PM motors, flexible coupling effect and mechatronic system are introduced.

A. Mathematic Model of the DIW-PM Motors

The following nonlinear equations of DIW-PM motors are used to characterize the mathematical model in the d/q coordinate [24]

$$D_E\ddot{q}_R(t) + W_1(q_{Mg}(t))\dot{q}_R(t) + W_2(q_{Mg}(t)) + R_e\dot{q}_R(t) = u_R \tag{1}$$

$$D_M\ddot{q}_{Mg}(t) - T_{Edq} + B_M\dot{q}_{Mg}(t) = u_M \tag{2}$$

$$\begin{cases} \dot{q}_R(t) = [\,\dot{q}_{rf} \quad \dot{q}_{rr}\,] = [\,i_{df} \quad i_{qf} \quad i_{dr} \quad i_{qr}\,]^T \\ u_R = [\,u_{df} \quad u_{qf} \quad u_{dr} \quad u_{qr}\,]^T \\ \dot{q}_{Mg} = [\,\dot{q}_{mfg}(\dot{q}_{mf},\dot{q}_{mrg}) \quad \dot{q}_{mrg}(\dot{q}_{mr},\dot{q}_{mfg})\,]^T \\ u_M = [\,u_{mf} \quad u_{mr}\,]^T = -[\,T_{lf} \quad T_{lr}\,]^T \\ T_{Edq} = \begin{bmatrix} T_{ef} \\ T_{er} \end{bmatrix} = 1.5\left(\begin{bmatrix} \lambda_f i_{qf} & 0 \\ 0 & \lambda_r i_{qr} \end{bmatrix} \right. \\ \qquad \left. + \begin{bmatrix} L_{df} - L_{qf} & 0 \\ 0 & L_{dr} - L_{qr} \end{bmatrix} \begin{bmatrix} i_{df} i_{qf} & 0 \\ 0 & i_{dr} i_{qr} \end{bmatrix} \right) \begin{bmatrix} p_f \\ p_r \end{bmatrix} \end{cases} \tag{3}$$

$$\begin{cases} D_E = \mathrm{diag}\{L_{df}, L_{qf}, L_{dr}, L_{qr}\} \\ D_M = \mathrm{diag}\{D_{mf}, D_{mr}\} \end{cases}$$

$$W_2 = \begin{bmatrix} 0 & 0 & 0 & 0 \\ 0 & \lambda_f p_f \dot{q}_{mfg} & 0 & 0 \\ 0 & 0 & 0 & 0 \\ 0 & 0 & 0 & \lambda_r p_r \dot{q}_{mrg} \end{bmatrix}$$

$$W_1 = \begin{bmatrix} 0 & -L_{qf} p_f \dot{q}_{mfg} & 0 & 0 \\ L_{df} p_f \dot{q}_{mfg} & 0 & 0 & 0 \\ 0 & 0 & 0 & -L_{qr} p_r \dot{q}_{mrg} \\ 0 & 0 & L_{dr} p_r \dot{q}_{mrg} & 0 \end{bmatrix} \tag{4}$$

where T_{Edq} is the electromagnetic torque, $q_R(t)$ represents electric charge under the dq coordinate and $q_{Mg}(t)$ is mechanical angel of motors with rigid coupling, R_e represents the resistance, L_d and L_q represent the inductance of DIW-PM motors in dq coordinate, p_f and p_r are the pole pairs of in-wheel motor #I and in-wheel motor #II, respectively, and T_{lf} and T_{lr} represent load torque of DIW-PM motors. Additionally, define the subscripts f and r, respectively, for the variables of the #I and #II in-wheel motors. In addition to representing the front and rear in-wheel motors, #I and #II can also represent the left and right in-wheel motors, respectively.

B. Modeling of Flexible Coupling Effect

Generally, due to the flexible coupling effect in the DD system which stemming from the inherent elasticity of components [1], the speed of the multiple in-wheel PM motors can be affect in depth. And at the mechanical junction of the coupling, shaft torque is generated, causing vehicle deviating from the intended route, intense vibration of the in-wheel motor, tire slippage, and other phenomena. This significantly impacts the steady-state accuracy and dynamic error of the control system. Consequently, in order to simulate such flexible coupling effect, it can be conceptualized as a mechatronic system comprising DIW-PM motors linked to a rigid construction.

The shaft torque produced by the coupling can be ignored if the DIW-PM motors are fully synchronized. Therefore, the speed of DIW-PM motors can be decomposed into the synchronous speed and speed difference generated by the coupling shaft torque. Define the shaft torque T_{sf} and T_{sr} through force analysis of generalized Hooke law, and the model can be rewrite as follows:

$$\begin{cases} T_{sf}(\dot{q}_{mfg}, \dot{q}_{mrg}) = r_1^2 \int_0^\infty (\dot{q}_{mrg} - \dot{q}_{mfg}) d\tau, T_{sr}(\dot{q}_{mfg}, \dot{q}_{mrg}) \\ \quad = r_2^2 \int_0^\infty (\dot{q}_{mfg} - \dot{q}_{mrg}) d\tau \\ \dot{q}_{mfg}(\dot{q}_{mf}, \dot{q}_{mrg}) = \dot{q}_{mf} - \dfrac{1}{D_{mf}} \int \dfrac{T_{sf}(\dot{q}_{mfg}, \dot{q}_{mrg})}{N_{sf}} d\tau \\ \quad = \dot{q}_{mf} - \dfrac{\Delta\omega}{D_{mf}} \\ \dot{q}_{mrg}(\dot{q}_{mr}, \dot{q}_{mfg}) = \dot{q}_{mr} - \dfrac{1}{D_{mr}} \int \dfrac{T_{sr}(\dot{q}_{mfg}, \dot{q}_{mrg})}{N_{sr}} d\tau \\ \quad = \dot{q}_{mr} + \dfrac{1}{D_{mr}} \int \dfrac{T_{sf}(\dot{q}_{mfg}, \dot{q}_{mrg})}{N_{sf}} d\tau = \dot{q}_{mr} + \dfrac{\Delta\omega}{D_{mr}} \end{cases} \tag{5}$$

where the diameter of the gear pulley $2r_1$, $2r_2$ are equivalent to 78.79 millimeter, D_{mf} and D_{mr} are the nominal inertia of DIW-PM motors, q_{mf} and q_{mr} are assumed to be mechanical angles that are perfectly synchronized when two motors are not rigidly connected, and N_{sf}, N_{sr} are represented the proportion of shaft torque transmission.

C. Mechatronic System Modeling

The EL model serves as a comprehensive framework for characterizing nonlinear physical systems by accounting for the interaction between mechanical and electromagnetic energy. It adeptly manages the conversion of these energies, amalgamates the dynamic and electrical aspects of mechatronic system, and formulates a cohesive mathematical model. Consequently, the EL formula is used to model the mechatronic system of the 1/2 DD system. And generally, EL formula is expressed as [25]

$$\frac{d}{dt}\left(\frac{\partial L_D}{\partial \dot{q}}(q(t), \dot{q}(t))\right) - \frac{\partial L_D}{\partial q}(q(t), \dot{q}(t)) = Q \tag{6}$$

where the Lagrangian function L_D of the mechatronic system, which equals to the difference between kinetic energy K and potential energy P, is defined as

$$L_D(q(t), \dot{q}(t)) = K(q(t), \dot{q}(t)) - P(q(t)) \tag{7}$$

where kinetic energy K, composed of magnetic field co-energy and mechanical kinetic energy, can be expressed as

$$K(q(t), \dot{q}(t)) = \frac{1}{2} q(t) D(q(t)) \dot{q}(t). \tag{8}$$

Furthermore, the variable $q(t)$ in formula (6) is defined as follows:

$$\begin{cases} \dot{q}(t) = \left[\dot{q}_E^T(t) \quad \dot{q}_{Mg}(t)\right]^T, \dot{q}_{mf} = \dot{q}_{mr} \\ \dot{q}_E(t) = \left[\dot{q}_{ef} \quad \dot{q}_{er}\right]^T = [i_{\alpha f} \quad i_{\beta f} \quad i_{\alpha r} \quad i_{\beta r}]^T \\ \dot{q}_{Mg} = [\dot{q}_{mfg}(\dot{q}_{mf},\dot{q}_{mrg}) \quad \dot{q}_{mrg}(\dot{q}_{mr},\dot{q}_{mfg})]^T \\ \quad = [\omega_{mfg}(\omega_{mf},\omega_{mrg}) \quad \omega_{mrg}(\omega_{mr},\omega_{mfg})]^T \end{cases} \tag{9}$$

where $q_E(t)$ represents electric charge of DIW-PM motors in the $\alpha\beta$ coordinate. And the Q is a generalized input vector that

encompasses disturbances and external inputs from the mechanical and motor sides, which is obtained as

$$\begin{cases} Q = u_D + Q_{dg} - \dfrac{\partial F_D}{\partial \dot{q}}, \\ u_D = \left[u_R^T \quad u_M\right]^T = \left[u_{df} \quad u_{qf} \quad u_{dr} \quad u_{qr} \quad u_M\right]^T \\ F_D(\dot{q}) = \dfrac{1}{2}\dot{q}_E^T R_e \dot{q}_E + \dfrac{1}{2} B_M \dot{q}_{Mg}^2, R_e = \mathrm{diag}\{r_{sf} \quad r_{sf} \quad r_{sr} \quad r_{sr}\} \\ Q_{dg} = [Q_{dfg} \quad Q_{drg}]^T = -[T_{sf}(q_{mfg}.q_{mrg}) \quad T_{sr}(q_{mfg}.q_{mrg})]^T. \end{cases} \tag{10}$$

where the external disturbance Q_{dg} of dual motors is produced by the shaft torque coupled with the mechanical system, which is closely associated with the mechanical angels of the dual motors. The input vector u_D consists of motor side voltage and load, and mechatronic dissipation function F_D is generated by resistance and damping.

Moreover, in the mechatronic system, the magnetic field co-energy is exclusively generated by the DIW-PM motors, which is defined by the combination of (1) and (3) and is expressed as [26]

$$K_E\left(\dot{q}_E(t), q_{Mg}(t)\right) = \sum_{i=1}^{n_E} \int_0^{\dot{q}_i} \lambda_i(\dot{q}_i) d\dot{q}_i \tag{11}$$

where the numbers of windings n_E equals four, and $\lambda = [\lambda_f \ \lambda_r]$ express the magnetic linkage of the DIW-PM motors.

On the other hand, as illustrated in [26], formula (2) and (7) can be combined to define the mechanical kinetic energy as follows:

$$K_M\left(\dot{q}_{Mg}(t)\right) = \frac{1}{2} D_{mf} \dot{q}_{mfg}^2 + \frac{1}{2} D_{mr} \dot{q}_{mrg}^2 = \frac{1}{2} D_M \dot{q}_{Mg}^2. \tag{12}$$

Therefore, the Lagrangian function, where the potential energy P is zero due to the uniform assignment of magnetic resistance, can be described as follows by combining (7), (11), and (12)

$$L_D = \frac{1}{2} D_M \dot{q}_{Mg}^2(t) + \sum_{i=1}^{n_E} \int_0^{\dot{q}_i} \lambda_i(\dot{q}_i) d\dot{q}_i. \tag{13}$$

In essence, the EL formula of mechatronic, obtained by combining (13) and formula (6), remains an independent set of electrical and mechanical equations. However, the cooperative control of mechatronic system needs to take into account not only the electrical equation to achieve current loop tracking, but also the reduction of the adverse effects of coupling shaft torque in order to achieve synchronized control of the DIW-PM motors. Consequently, in order to produce a nonlinear equation that integrated mechanical and electrical elements, EL formula can be translated into Hamiltonian equations. So, a n-dimensional generalized momentum vector and Hamiltonian function H are defined as

$$p = \frac{\partial L_D(q(t), \dot{q}(t))}{\partial \dot{q}} = D(q(t))\dot{q}(t) \tag{14}$$

$$H(q(t), \dot{q}(t)) = K(q(t), \dot{q}(t)) + P(q(t)) = L_D(q(t), \dot{q}(t)) \tag{15}$$

where the function H is the sum of the kinetic energy and potential energy of the mechatronic system. Besides, defining the input is Q and output is u, and substituting (14) and (15) into (6), the general formula of the Hamilton can be organized as

$$\dot{q} = \frac{\partial H(q,p)}{\partial p}, \dot{p} = \frac{\partial H(q,p)}{\partial q} + Q(q,p), \ y = \dot{q} \tag{16}$$

and the typical nonlinear formula of the mechatronic system can be expressed as

$$\dot{x} = f(x) + g(x)Q(x), \ y = h(x). \tag{17}$$

Accordingly, a combined expression of electrical and mechanical equations based on EL model is established by generalizing the general formula of (16) based on (17):

$$\dot{x} = [J(x) - R(x)]\frac{\partial H(x)}{x} + g(x)Q(x), \ y = g^{\mathrm{T}}(x)\frac{\partial H(x)}{\partial x} \tag{18}$$

where $J(x) = -J^{\mathrm{T}}(x)$ is the interconnection matrix representing the coupling relationship of internal parameters, while $R(x) = R^{\mathrm{T}}(x)$ represents the matrix of friction damping coefficient, which signifies the dissipation of the mechatronic system. In fact, the DIW-PM motors' internal damping is essentially insignificant and can be disregarded, while the external damping can be considered as a part of load torque input, therefore B_M is zero. In summary, by substituting (1), (2), (5) and (10) into (18), the interconnection equation for electrical and mechanical is obtained as

$$\begin{cases} \dot{x}^T = [J(x) - R(x)]\left[\dot{q}_{rf} \ \ \dot{q}_{mfg}(\dot{q}_{mf}.\dot{q}_{mrg}) \ \ \dot{q}_{rr} \ \ \dot{q}_{mrg}(\dot{q}_{mr}.\dot{q}_{mfg})\right]^T \\ \qquad + g\left[u_{Rf} \ \ u_{mf} + Q_{dfg} \ \ u_{Rr} \ \ u_{mr} + Q_{drg}\right]^T \\ y = g^{\mathrm{T}}\dfrac{\partial H(x)}{\partial x} = \left[\dot{q}_{rf} \ \ \dot{q}_{mfg}(\dot{q}_{mf}.\dot{q}_{mrg}) \ \ \dot{q}_{rr} \ \ \dot{q}_{mrg}(\dot{q}_{mr}.\dot{q}_{mfg})\right]^{\mathrm{T}} \end{cases} \tag{19}$$

$$\begin{cases} R(x) = \mathrm{diag}\{r_{sf}, r_{sf}, 0, r_{sr}, r_{sr}, 0\}, g(x) = I_6 \\ D = \mathrm{diag}\{L_{df}, L_{qf}, D_{mf}, L_{dr}, L_{qr}, L_{qr}, D_{mr}\} \\ x = [x_1 \quad x_2 \quad x_3 \quad x_4 \quad x_5 \quad x_6]^{\mathrm{T}} \\ \quad = D\left[\dot{q}_{rf} \quad \dot{q}_{mfg}(\dot{q}_{mf}.\dot{q}_{mrg}) \quad \dot{q}_{rr} \quad \dot{q}_{mrg}(\dot{q}_{mr}.\dot{q}_{mfg})\right]^{\mathrm{T}} \\ H(x) = \dfrac{1}{2} x^{\mathrm{T}} D^{-1} x \end{cases} \tag{20}$$

$$\begin{cases} \mathrm{A}_{3\times3} = \begin{bmatrix} 0 & 0 & p_f x_2 \\ 0 & 0 & -p_f(x_1 + \lambda_f) \\ -p_f x_2 & p_f(x_1 + \lambda_f) & 0 \end{bmatrix} \\ J(x) = \begin{bmatrix} \mathrm{A}_{3\times3} & 0_{3\times3} \\ 0_{3\times3} & B_{3\times3} \end{bmatrix}, B_{3\times3} = \begin{bmatrix} 0 & 0 & p_r x_5 \\ 0 & 0 & -p_r(x_4 + \lambda_r) \\ -p_r x_5 & p_r(x_4 + \lambda_r) & 0 \end{bmatrix}. \end{cases} \tag{21}$$

III. Principle of Euler-Lagrange-Model Based Torque Assignment Control

In order to achieve the cooperation of the DIW-PM motors, the ELM-TA control strategy is proposed as shown in Fig. 3. Through the EL model, real-time allocation of electromagnetic

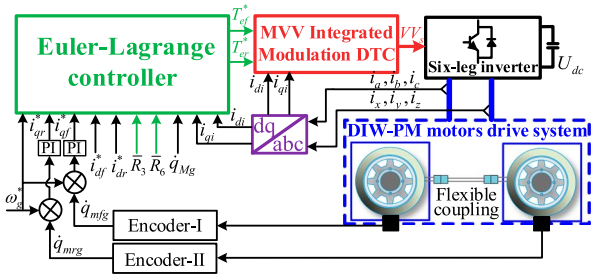

Fig. 3. ELM-TA control for DIW-PM motors drive system.

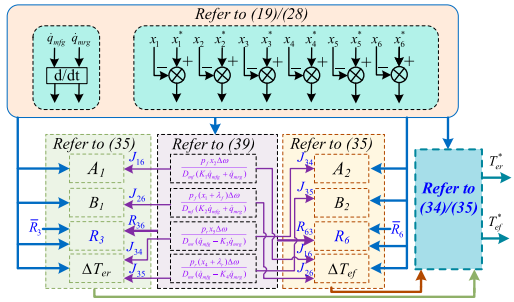

Fig. 4. Block diagram of the EL controller.

torque is achieved, allowing DIW-PM motors cooperation under various circumstances. Furthermore, the MVV modulation based integrated torque control is used after the assigned electromagnetic torque has been received, and the coupling DIW-PM motors can be driven by selecting the voltage vector through torque and magnetic linkage.

In order to ensure that (18) of the DIW-PM mechatronic system is asymptotically stabilized close to the desired equilibrium point x^*, the method of reconstructing the interconnection and friction damping coefficient matrices is used for the ELM-TA control law. It is assumed that there exists a feedback law $u = \beta(x)$ such that the mechatronic system reaches a minimum value at the expected equilibrium point x^* through an expectation function $H_d(x)$ (e.g., $H_d(x) > H_d(x^*)$ for any $x \neq x^*$ in a neighborhood of x^*). If $x^* - x$ tends to zero, the Hamiltonian function $H(x)$ can quickly converge to $H_d(x)$ by the interconnection and friction damping injection. And the closed-loop system can be described as

$$\dot{x} = [J_d(x) - R_d(x)]\frac{\partial H_d(x)}{\partial x} \tag{22}$$

where $J_d(x)$ and $R_d(x)$ are the desired interconnection matrix and friction damping coefficient matrix, respectively, satisfying the following condition:

$$\begin{aligned} J(\boldsymbol{x}) + J_a(\boldsymbol{x}) &= -[J(\boldsymbol{x}) + J_a(\mathbf{x})]^{\mathrm{T}} = J_d, R(x) + R_a(x) \\ &= [R(x) + R_a(x)]^{\mathrm{T}} = R_d \end{aligned} \tag{23}$$

where $J_a(x)$ and $R_a(x)$ are self-set injection matrix. And generally, if a feedback law $Q(x) = \beta(x)$ can be identified given $J(x)$, $R(x)$, $H(x)$, $g(x)$ and expected equilibrium point x^*, then $J_a(x)$, $R_a(x)$ and vector function $K(x)$ satisfy the following equations [27]:

$$\begin{aligned} &\{J(x) + J_a(x) - [R(x) + R_a(x)]\}K(x) \\ &\quad = -[J_a(x) - R_a(x)]\frac{\partial H(x)}{\partial x} + g(x)\beta(x) \end{aligned} \tag{24}$$

$$\begin{aligned} \frac{\partial K(x)}{\partial x} &= \left[\frac{\partial K(x)}{\partial x}\right]^{\mathrm{T}}, \frac{\partial K(x)}{\partial x}\bigg|_{x=x^*} > -\frac{\partial^2 H(x)}{\partial x^2}\bigg|_{x=x^*}, K(x^*) \\ &= -\frac{\partial H}{\partial x}(x^*), K(x) = -D^{-1}x^* \end{aligned} \tag{25}$$

where $H_a(x)$ is self-set injection Hamiltonian function, which represents the energy injected into the mechatronic system by designing a law to make the system tend towards the desired equilibrium point.

$$H_d(x) = H(x) + H_a(x). \tag{26}$$

A. Design of the Euler-Lagrange Controller

Based on the Euler-Lagrange model, the EL controller shown in Fig. 4 is constructed by taking the external disturbances, such as sudden load changes, internal torque fluctuations, and system state variables., etc., as the influencing factors of torque assignment. And, the allocated torque will be given as the reference torque of the MVV modulation DTC. For the EL controller, by enforcing stable voltage tracking, integrating the drive through rapid torque output, and minimizing the time for adverse movements such as slipping are all essential to enable the swift response of DIW-PM motors to achieve synchrony.

Therefore, $i_d = i_d^* = 0$ and $i_q = i_q^*$ are selected as the expected equilibrium points of the mechatronic system

$$\begin{aligned} x^* &= [x_1^* \quad x_2^* \quad x_3^* \quad x_4^* \quad x_5^* \quad x_6^*]^{\mathrm{T}} \\ &= [0 \quad L_{qf} i_{qf}^* \quad D_{mf}\omega_g^* \quad 0 \quad L_{qr} i_{qr}^* \quad D_{mr}\omega_g^*]^{\mathrm{T}} \end{aligned} \tag{27}$$

$$\begin{cases} u_{df}^* = \dfrac{R_{sf}}{L_{df}}x_1^* - \dfrac{p_f}{D_{mf}}x_2^* x_3^*, u_{dr}^* = \dfrac{R_{sr}}{L_{dr}}x_4^* - \dfrac{p_r}{D_{mr}}x_5^* x_6^* \\ u_{qf}^* = \dfrac{R_{sf}}{L_{qf}}x_2^* - \dfrac{p_f}{D_{mf}}x_1^* x_3^* + \dfrac{p_f\lambda_f}{D_{mf}}x_3^*, u_{qr}^* = \dfrac{R_{sr}}{L_{qr}}x_5^* - \dfrac{p_r}{D_{mr}}x_4^* x_6^* + \dfrac{p_r\lambda_r}{D_{mr}}x_6^* \end{cases} \tag{28}$$

where ω_g^* is the predetermined velocity. Due to the existing coupling, the expected Hamiltonian function, interconnection and friction damping coefficient matrices are organized as

$$H_d(x) = \frac{1}{2}(x - x^*)^{\mathrm{T}} D^{-1}(x - x^*), R_a = \mathrm{diag}(R_1, R_2, R_3, R_4, R_5, R_6) \tag{29}$$

$$J_a(x) = \begin{bmatrix} 0 & -J_{12} & J_{13} & 0 & 0 & J_{16} \\ J_{12} & 0 & -J_{23} & 0 & 0 & -J_{26} \\ -J_{13} & J_{23} & 0 & J_{34} & -J_{35} & 0 \\ 0 & 0 & -J_{34} & 0 & -J_{45} & J_{46} \\ 0 & 0 & J_{35} & J_{45} & 0 & -J_{56} \\ -J_{16} & J_{26} & 0 & -J_{46} & J_{56} & 0 \end{bmatrix}. \tag{30}$$

And, by substituting (20), (21), (27), and (29) into (24), the closed-loop control law can be expressed as

$$\begin{cases} u_{df}=u_{df}^*-\dfrac{R_1}{L_{df}}x_1-\left(\dfrac{J_{12}}{L_{qf}}+\dfrac{p_f x_3^*}{D_{mf}}\right)(x_2-x_2^*) \\ \quad +\dfrac{J_{13}}{D_{mf}}(x_3-x_3^*)+\dfrac{J_{16}}{D_{mr}}(x_6-x_6^*) \\ u_{qf}=u_{qf}^*+\left(\dfrac{J_{12}}{L_{df}}+\dfrac{p_f x_3^*}{D_{mf}}\right)x_1-\dfrac{R_2}{L_{qf}}(x_2-x_2^*) \\ \quad -\dfrac{J_{23}}{D_{mf}}(x_3-x_3^*)-\dfrac{J_{26}}{D_{mr}}(x_6-x_6^*),-T_{Lf}-\dfrac{T_{sf}(\dot{q}_{mfg},\dot{q}_{mrg})}{N_{sf}} \\ =-T_{ef}^*-\left(\dfrac{J_{13}}{L_{df}}+\dfrac{p_f x_2^*}{L_{qf}}\right)(x_1-x_1^*) \\ \quad +\left(\dfrac{J_{23}}{L_{qf}}+\dfrac{p_f x_1^*}{L_{df}}\right)(x_2-x_2^*)-\dfrac{R_3}{D_{mf}}(x_3-x_3^*)+\dfrac{J_{34}}{L_{dr}}x_4-\dfrac{J_{35}}{L_{qr}}(x_5-x_5^*) \\ u_{dr}=u_{dr}^*-\dfrac{R_4}{L_{dr}}x_4-\left(\dfrac{J_{45}}{L_{qr}}+\dfrac{p_r x_6^*}{D_{mr}}\right)(x_5-x_5^*) \\ \quad +\dfrac{J_{46}}{D_{mr}}(x_6-x_6^*)-\dfrac{J_{34}}{D_{mf}}(x_3-x_3^*) \\ u_{qf}=u_{qr}^*+\left(\dfrac{J_{45}}{L_{dr}}+\dfrac{p_r x_6^*}{D_{mr}}\right)x_4-\dfrac{R_5}{L_{qr}}(x_5-x_5^*)-\dfrac{J_{56}}{D_{mr}}(x_6-x_6^*) \\ \quad +\dfrac{J_{35}}{D_{mf}}(x_3-x_3^*),-T_{Lr}-\dfrac{T_{sr}(\dot{q}_{mfg},\dot{q}_{mrg})}{N_{sr}} \\ =-T_{er}^*-\left(\dfrac{J_{46}}{L_{dr}}+\dfrac{p_r x_5^*}{L_{qr}}\right)(x_4-x_4^*) \\ \quad +\left(\dfrac{J_{56}}{L_{qr}}+\dfrac{p_r x_4^*}{L_{dr}}\right)(x_5-x_5^*)-\dfrac{R_6}{D_{mr}}(x_6-x_6^*)-\dfrac{J_{16}}{L_{df}}x_1+\dfrac{J_{26}}{L_{qf}}(x_2-x_2^*). \end{cases} \tag{31}$$

Moreover, combining the current constraints mentioned earlier, with stable voltage tracking as the goal (e.g., $u_d = u_d^*$ and $u_q = u_q^*$). By substituting the goal into (29), the EL controller with various self-set injection coefficients can be derived as:

$$\begin{cases} -\dfrac{R_1}{L_{df}}x_1-\left(\dfrac{J_{12}}{L_{qf}}+\dfrac{p_f x_3^*}{D_{mf}}\right)(x_2-x_2^*)+\dfrac{J_{13}}{D_{mf}}(x_3-x_3^*)+\dfrac{J_{16}}{D_{mr}}(x_6-x_6^*)=0 \\ \left(\dfrac{J_{12}}{L_{df}}+\dfrac{p_f x_3^*}{D_{mf}}\right)x_1-\dfrac{R_2}{L_{qf}}(x_2-x_2^*)-\dfrac{J_{23}}{D_{mf}}(x_3-x_3^*)-\dfrac{J_{26}}{D_{mr}}(x_6-x_6^*)=0 \\ -\dfrac{R_4}{L_{dr}}x_4-\left(\dfrac{J_{45}}{L_{qr}}+\dfrac{p_r x_6^*}{D_{mr}}\right)(x_5-x_5^*)+\dfrac{J_{46}}{D_{mr}}(x_6-x_6^*)-\dfrac{J_{34}}{D_{mf}}(x_3-x_3^*)=0 \\ \left(\dfrac{J_{45}}{L_{dr}}+\dfrac{p_r x_6^*}{D_{mr}}\right)x_4-\dfrac{R_5}{L_{qr}}(x_5-x_5^*)-\dfrac{J_{56}}{D_{mr}}(x_6-x_6^*)+\dfrac{J_{35}}{D_{mf}}(x_3-x_3^*)=0 \end{cases} \tag{32}$$

where (33) includes current term, coupling term of speed and current, speed term and various self-set injection coefficients that need to be tuned. Therefore, in order to achieve the separation of speed term and current term in (32) and modify the coefficient of the speed to achieve speed tracking, the self-set injection can be deduced by setting the coefficient of the current term to zero as follows:

$$\begin{cases} R_1=0, J_{12}=\dfrac{-L_{qf}p_f x_3^*}{D_{mf}}, R_2=0, R_4=0 \\ J_{45}=\dfrac{-L_{qr}p_r x_6^*}{D_{mr}}, R_5=0, J_{13}=\dfrac{D_{mf}J_{16}(x_6-x_6^*)}{D_{mr}(x_3^*-x_3)} \\ J_{23}=\dfrac{D_{mf}J_{26}(x_6^*-x_6)}{D_{mr}(x_3-x_3^*)}, J_{46}=\dfrac{D_{mr}J_{34}(x_3-x_3^*)}{D_{mf}(x_6-x_6^*)} \\ J_{56}=\dfrac{D_{mr}J_{35}(x_3-x_3^*)}{D_{mf}(x_6-x_6^*)}. \end{cases} \tag{33}$$

Eventually, by substituting (33), (15) into (32), the EL controller can be obtained as (34) and shown in Fig. 4, where the ΔT_{er}, ΔT_{ef} can represent the torque impact caused by coupling from each other:

$$\begin{cases} T_{ef}^*=T_{ef}-D_{mf}\dfrac{d\dot{q}_{mfg}}{dt}-A_1x_1+B_1(x_2-x_2^*)-\dfrac{R_3}{D_{mf}}(x_3-x_3^*) \\ \quad +\Delta T_{er}, \Delta T_{er}=\dfrac{J_{34}}{L_{dr}}(x_4-x_4^*)-\dfrac{J_{35}}{L_{qr}}(x_5-x_5^*) \\ T_{er}^*=T_{er}-D_{mr}\dfrac{d\dot{q}_{mrg}}{dt}-A_2x_4+B_2(x_5-x_5^*)-\dfrac{R_6}{D_{mr}}(x_6-x_6^*) \\ \quad +\Delta T_{ef}, \Delta T_{ef}=-\dfrac{J_{16}}{L_{df}}(x_1-x_1^*)+\dfrac{J_{26}}{L_{qf}}(x_2-x_2^*) \\ A_1=\left(\dfrac{D_{mf}J_{16}(x_6-x_6^*)}{D_{mr}L_{df}(x_3^*-x_3)}+\dfrac{p_f x_2^*}{L_{qf}}\right) \\ B_1=\left(\dfrac{D_{mf}J_{26}(x_6^*-x_6)}{D_{mr}L_{qf}(x_3-x_3^*)}+\dfrac{p_f x_1^*}{L_{df}}\right) \\ A_2=\left(\dfrac{D_{mr}J_{34}(x_3-x_3^*)}{D_{mf}L_{dr}(x_6-x_6^*)}+\dfrac{p_r x_5^*}{L_{qr}}\right) \\ B_2=\left(\dfrac{D_{mr}J_{35}(x_3-x_3^*)}{D_{mf}(x_6-x_6^*)L_{qr}}+\dfrac{p_r x_4^*}{L_{dr}}\right). \end{cases} \tag{34}$$

B. Interconnection and Damping Parameters Calculation

According to control law described in (35), there exists six interconnection and friction damping coefficients that interact with each other and need to be tuned. Therefore, by establishing constraint conditions based on the desired Hamiltonian function, a dynamic tuning strategy is proposed which can reduce the number of self-set injection coefficients and improve the robustness of the algorithm. First, the closed-loop equation can be obtained by substituting (20), (21), and (29) into (22):

$$\begin{cases} \dot{\boldsymbol{x}}=\begin{bmatrix} C_{3\times3} & D_{3\times3} \\ E_{3\times3} & F_{3\times3} \end{bmatrix} \\ D^{-1}\begin{bmatrix} x_1-x_1^* & x_2-x_2^* & x_3-x_3^* & x_4-x_4^* & x_5-x_5^* & x_6-x_6^* \end{bmatrix}^T \\ J_{\mathrm{d}}(x)-R_{\mathrm{d}}(x)=\begin{bmatrix} C_{3\times3} & D_{3\times3} \\ E_{3\times3} & F_{3\times3} \end{bmatrix} \end{cases} \tag{35}$$

$$\begin{cases} C_{3\times3}=\begin{bmatrix} -r_{sf} & -J_{12} & J_{13}+p_f x_2 \\ J_{12} & -r_{sf} & -J_{23}-p_f(x_1+\lambda_f) \\ -J_{13}-p_f x_2 & J_{23}+p_f(x_1+\lambda_f) & -R_3 \end{bmatrix} \\ D_{3\times3}=\begin{bmatrix} 0 & 0 & J_{16} \\ 0 & 0 & -J_{26} \\ J_{34} & -J_{35} & 0 \end{bmatrix} \\ E_{3\times3}=\begin{bmatrix} 0 & 0 & -J_{34} \\ 0 & 0 & J_{35} \\ -J_{16} & J_{26} & 0 \end{bmatrix} \\ F_{3\times3}=\begin{bmatrix} -r_{sr} & -J_{45} & J_{46}+p_r x_5 \\ J_{45} & -r_{sr} & -J_{56}-p_r(x_4+\lambda_r) \\ -J_{46}-p_r x_5 & J_{56}+p_r(x_4+\lambda_r) & -R_6 \end{bmatrix}. \end{cases} \tag{36}$$

In order to reduce the coupling effect caused by mechatronic system, we not only expect (35) to be locally minimized at the equilibrium point, but also to achieve the decoupling of the state variables in the dynamic process before (35) reaches the equilibrium point. Therefore, by comparing (19), (28) with (35), and substituting (17) into (35), the constraint condition can be obtained as

$$\begin{cases} (J_{13}+p_f x_2)\left(\dot{q}_{mf}-\dfrac{\Delta\omega}{D_{mf}}\right)+J_{16}\dot{q}_{mrg}=p_f x_2\dot{q}_{mf} \\ [-J_{23}-p_f(x_1+\lambda_f)]\left(\dot{q}_{mf}-\dfrac{\Delta\omega}{D_{mf}}\right)-J_{26}\dot{q}_{mrg}=-p_f(x_1+\lambda_f)\dot{q}_{mf} \\ (J_{46}+p_r x_5)\left(\dot{q}_{mr}+\dfrac{\Delta\omega}{D_{mf}}\right)-J_{34}\dot{q}_{mfg}=p_r x_5\dot{q}_{mr} \\ [-J_{56}-p_r(x_4+\lambda_r)]\left(\dot{q}_{mr}+\dfrac{\Delta\omega}{D_{mf}}\right)+J_{35}\dot{q}_{mfg}=-p_r(x_4+\lambda_r)\dot{q}_{mr}. \end{cases} \tag{37}$$

Furthermore, by considering (37) and (33), the dynamic solution of interconnection coefficients can be expressed as

$$\begin{cases} J_{16}=\dfrac{p_f x_2\Delta\omega}{D_{mf}(K_1\dot{q}_{mfg}+\dot{q}_{mrg})}, J_{26}=\dfrac{p_f(x_1+\lambda_f)\Delta\omega}{D_{mf}(K_2\dot{q}_{mfg}+\dot{q}_{mrg})} \\ J_{34}=\dfrac{p_r x_5\Delta\omega}{D_{mr}(\dot{q}_{mfg}-K_3\dot{q}_{mrg})}, J_{35}=\dfrac{p_r(x_4+\lambda_r)\Delta\omega}{D_{mr}(\dot{q}_{mfg}-K_4\dot{q}_{mrg})} \\ K_1=\dfrac{D_{mf}(x_6-x_6^*)}{D_{mr}(x_3^*-x_3)}, K_2=\dfrac{D_{mf}(x_6^*-x_6)}{D_{mr}(x_3-x_3^*)} \\ K_3=\dfrac{D_{mr}(x_3-x_3^*)}{D_{mf}(x_6-x_6^*)}, K_4=\dfrac{D_{mr}(x_3-x_3^*)}{D_{mf}(x_6-x_6^*)}. \end{cases} \tag{38}$$

Moreover, it can be seen from (34) that the correlation between the friction damping coefficients and speed is significant, leading to the division of the friction damping coefficients into dynamic solution and tuning solution. The dynamic solution counteracts the speed coupling effect, while the tuning solution governs the synchronous performance of the dual motors. Consequently, similar to the adjust of the interconnection coefficients, the dynamic solution of friction damping coefficients can

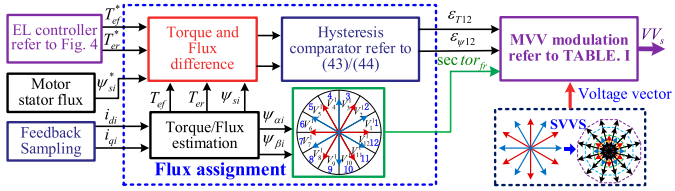

Fig. 5. Block diagram of the MVV.

be expressed as

$$\begin{cases} \mathrm{W}_1=-p_f x_2\dfrac{(x_1-x_1^*)}{L_{df}}+p_f(x_1+\lambda_f)\dfrac{(x_2-x_2^*)}{L_{qf}}, \\ \mathrm{W}_2=-p_r x_5\dfrac{(x_4-x_4^*)}{L_{dr}}+p_r(x_4+\lambda_r)\dfrac{(x_5-x_5^*)}{L_{qr}} \\ \mathrm{W}_1=(-J_{13}-p_f x_2)\dfrac{(x_1-x_1^*)}{L_{df}}+(J_{23}+p_f(x_1+\lambda_f))\dfrac{(x_2-x_2^*)}{L_{qf}} \\ \quad -\dfrac{R_3}{D_{mf}}(x_3-x_3^*)+J_{34}\dfrac{(x_4-x_4^*)}{L_{dr}}-J_{35}\dfrac{(x_5-x_5^*)}{L_{qr}} \\ \mathrm{W}_2=(-J_{46}-p_r x_5)\dfrac{(x_4-x_4^*)}{L_{dr}}+(J_{56}+p_r(x_4+\lambda_r))\dfrac{(x_5-x_5^*)}{L_{qr}} \\ \quad -\dfrac{R_6}{D_{mr}}(x_6-x_6^*)-J_{16}\dfrac{(x_1-x_1^*)}{L_{df}}+J_{26}\dfrac{(x_2-x_2^*)}{L_{qf}}. \end{cases} \tag{39}$$

Consequently, by considering (38), the dynamic solution is as follows:

$$\begin{cases} R_{36}=\dfrac{D_{mf}}{(x_3-x_3^*)}[-J_{16}K_1(i_{df}-i_{df}^*)+J_{26}K_2(i_{qf}-i_{qf}^*) \\ \quad +J_{34}(i_{dr}-i_{dr}^*)-J_{35}(i_{qr}-i_{qr}^*)] \\ R_{63}=\dfrac{D_{mr}}{(x_6-x_6^*)}[-J_{34}K_3(i_{dr}-i_{dr}^*)+J_{35}K_4(i_{qr}-i_{qr}^*) \\ \quad -J_{16}(i_{df}-i_{df}^*)+J_{26}(i_{qf}-i_{qf}^*)] \end{cases} \tag{40}$$

where R_{36} and R_{63} represent the derived dynamic solution. With the tuning solution, the friction damping coefficients can be expressed as

$$\begin{cases} R_3=R_{36}+\overline{R_3} \\ R_6=R_{63}+\overline{R_6}. \end{cases} \tag{41}$$

C. Multivoltage Vector Integrated Modulation DTC

As shown in Fig. 5, the multiple voltage vector (MVV) integrated modulation direct torque control (DTC) method [30] is adopted. The MVV integrated modulation DTC consists of flux assignment, space voltage vector synthetization (SVVS), and MVV modulation. The vector sector is determined from the flux feedback obtained from the observer, and the difference is compared with the hysteresis comparator threshold to generate the modulation signal.

Besides, based on the coupling of dual motor magnetic fields, the basic voltage vector of the dual motor is synthesized into 64 voltage vectors in the fundamental α_1-β_1 subspace, corresponding

TABLE I
SWITCH TABLE OF THE VOLTAGE VECTORS

Sector k (k = 1,3,5,7,9,11)	$\varepsilon_{T12}=11$	$\varepsilon_{T12}=10$	$\varepsilon_{T12}=01$	$\varepsilon_{T12}=00$
$\varepsilon\psi_{12}=11$	$V^1_{k+2}V^2_{k+3}$	$V^1_{k+2}V^2_{k-1}$	$V^1_{k-2}V^2_{k+3}$	$V^1_{k-2}V^2_{k-1}$
$\varepsilon\psi_{12}=10$	$V^1_{k+2}V^2_{k+5}$	$V^1_{k+2}V^2_{k-3}$	$V^1_{k-2}V^2_{k+5}$	$V^1_{k-2}V^2_{k-3}$
$\varepsilon\psi_{12}=01$	$V^1_{k+4}V^2_{k+3}$	$V^1_{k+4}V^2_{k-1}$	$V^1_{k-4}V^2_{k+3}$	$V^1_{k-4}V^2_{k-1}$
$\varepsilon\psi_{12}=00$	$V^1_{k+4}V^2_{k+5}$	$V^1_{k+4}V^2_{k-3}$	$V^1_{k-4}V^2_{k+5}$	$V^1_{k-4}V^2_{k-3}$
Sector k (k = 2,4,6,8,10,12)	$\varepsilon_{T12}=11$	$\varepsilon_{T12}=10$	$\varepsilon_{T12}=01$	$\varepsilon_{T12}=00$
$\varepsilon\psi_{12}=11$	$V^1_{k+3}V^2_{k+2}$	$V^1_{k+3}V^2_{k}$	$V^1_{k-1}V^2_{k+2}$	$V^1_{k-1}V^2_{k}$
$\varepsilon\psi_{12}=10$	$V^1_{k+3}V^2_{k+4}$	$V^1_{k+3}V^2_{k-4}$	$V^1_{k-1}V^2_{k+4}$	$V^1_{k-1}V^2_{k-4}$
$\varepsilon\psi_{12}=01$	$V^1_{k+5}V^2_{k+2}$	$V^1_{k+5}V^2_{k}$	$V^1_{k-3}V^2_{k+2}$	$V^1_{k-3}V^2_{k}$
$\varepsilon\psi_{12}=00$	$V^1_{k+5}V^2_{k+4}$	$V^1_{k+5}V^2_{k-4}$	$V^1_{k-3}V^2_{k+4}$	$V^1_{k-3}V^2_{k-4}$

to 64 switching states of the six half-bridges inverter and voltage vectors in Table I. Subsequently, by considering the modulation signal, sector signal, and composite sector rule, the most suitable voltage vector for controlling torque and magnetic linkage loop is selected.

And then, the sector judgment and space voltage vector synthetization are shown in Fig. 5, with the control function of flux assignment and switch table as follows:

$$\varepsilon_{T12}=\begin{cases}11, \left(T^*_{ef}-T_{ef}>0.001\right)\&\left(T^*_{er}-T_{er}>0.001\right)\\ 10, \left(T^*_{ef}-T_{ef}>0.001\right)\&\left(T^*_{er}-T_{er}<-0.001\right)\\ 01, \left(T^*_{ef}-T_{ef}<-0.001\right)\&\left(T^*_{er}-T_{er}>0.001\right)\\ 00, \left(T^*_{ef}-T_{ef}<-0.001\right)\&\left(T^*_{er}-T_{er}<-0.001\right)\end{cases} \tag{42}$$

D. Controller Stability Analysis

In order to verify the stability of the algorithm, the Lyapunov function is selected as

$$\begin{aligned}V_H(x)=H_d(x)=\frac{1}{2}\Bigg[&\frac{1}{L_{df}}\left(x_1-x_1^*\right)^2+\frac{1}{L_{qf}}\left(x_2-x_2^*\right)^2\\&+\frac{1}{D_{mf}}\left(x_3-x_3^*\right)^2+\frac{1}{L_{dr}}\left(x_4-x_4^*\right)^2+\frac{1}{L_{qr}}\left(x_5-x_5^*\right)^2\\&+\frac{1}{D_{mr}}\left(x_6-x_6^*\right)^2\Bigg]\end{aligned} \tag{44}$$

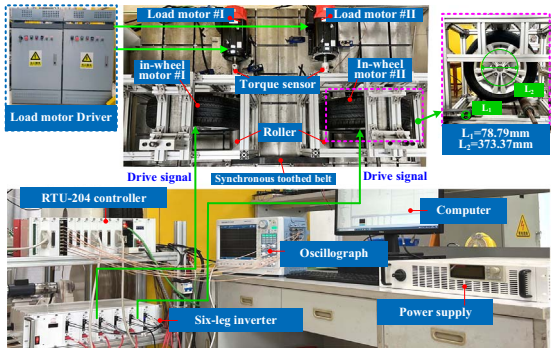

Fig. 6. experiment setups and platform.

which shows that $V_H(x)>0$, and according to (21)

$$\begin{aligned}\dot{V}_H(x)=\dot{H}_d(x)&=\left(\frac{\partial H_d(x)}{\partial x}\right)^T\dot{x}\\&=\left(\frac{\partial H_d(x)}{\partial x}\right)^T\left[J_d(x)-R_d(x)\right]\frac{\partial H_d(x)}{\partial x}.\end{aligned} \tag{45}$$

It is evident from substituting equations (20), (23), (29), (30) into (45) that setting R_3 and R_6 to be nonnegative will satisfy the negative semidefinite matrix of $J_d(x)$-$R_d(x)$

$$\begin{aligned}J_d(x)-R_d(x)=&-R_{sf}x_1^2-R_{sf}x_2^2-R_3x_3^2\\&-R_{sr}x_4^2-R_{sr}x_5^2-R_6x_6^2\le 0.\end{aligned} \tag{47}$$

Consequently, according to LaSalle's invariance principle, the system is asymptotically stable if the closed-loop is contained in the set $\{x\in \mathrm{R}^n|[\partial H_d/\partial x]^{\mathrm{T}}[J_d(x)\text{-}R_d(x)]\ \partial H_d/\partial x=0\}$ equal to $\{x^*\}$.

IV. EXPERIMENTAL VERIFICATION

In order to verify the effectiveness of the ELM-TA, the master-slave direct torque control (MSDTC), as shown in Fig. 1, is selected for comparison, where the slave torque is provided by the master motor #I. When facing different in-wheel motors with different parameters or power levels, simple torque commands cannot achieve speed synchronization. Therefore, a speed deviation compensation module is added to coordinate the output of the given electromagnetic torque in master-slave controller [28], [29].

Moreover, the DIW-PM motors mechatronic experimental platform is built and shown in Fig. 6. The experimental setup includes the RTU-204 controller, six-leg inverters, DIW-PM motors experimental platform and mechanical coupling device. It should be noted that the RTU-204 controller core integrates a TMS320F28346 microcontroller from Texas Instruments

$$\varepsilon_{\psi 12}=\begin{cases}11, \left(|\psi^*_{sf}|-|\psi_{sf}|>0.0001\right)\&\left(|\psi^*_{sr}|-|\psi_{sr}|>0.0001\right)\\ 10, \left(|\psi^*_{sf}|-|\psi_{sf}|>0.0001\right)\&\left(|\psi^*_{sr}|-|\psi_{sr}|<-0.0001\right)\\ 01, \left(|\psi^*_{sf}|-|\psi_{sf}|<-0.0001\right)\&\left(|\psi^*_{sr}|-|\psi_{sr}|>0.0001\right)\\ 00, \left(|\psi^*_{sf}|-|\psi_{sf}|<-0.0001\right)\&\left(|\psi^*_{sr}|-|\psi_{sr}|<-0.0001\right).\end{cases}, |\psi_{si}|=\sqrt{\psi^2_{\alpha i}+\psi^2_{\beta i}} \tag{43}$$

TABLE II
DIW-PM MOTORS PARAMETERS

Parameters	Value of Motor#I	Value of Motor#II	Parameters of Load Motor	Value
Flux linkage	0.049 Wb	0.05 2 Wb	Rated voltage	380 V
L_d	1.253 mH	0.928 mH	Rated power	5.5 kW
L_q	1.642 mH	0.928 mH	Rated torque	35 N·m
Rated speed	900 r/min	900 r/min	Rated speed	1500 r/min
Rated torque	68 N·m	70 N·m	Rated current	13 A
Stator resistance	0.1129 Ω	0.1469 Ω	Maximum speed	8 000 r/min
Pole of Pairs	25	17	Pole	4
Moment of inertia	1.398 kg·m^2	1 kg·m^2	Rated frequency	51.5 Hz
Proportional	0.5	0.3	Ingress protection	55
Integral	1.5	1.2	/	/

Incorporated, along with dedicated Xilinx FPGAs for distributed signal processing and PWM generation, operating at a configured frequency of 5 kHz. And, the load motor #I and load motor #II, powered by the load motor driver, are both asynchronous AC spindle servo motors. Besides, simulating the coupling of DIW-PM motors by engaging synchronous gear belts with gear belt pulleys, the forced synchronization of dual motors is ensured. In terms of loading, the load motor exerts direct force on the drum, which transfers to the motor via contact between the drum and tire. In the analysis of the Fig. 6, it is observed that the torque acting on the drum and in-wheel motor is directly proportional to their radii. Combining the diameter values marked in Fig. 6, the ratio of the torque on the drum T_R to the torque on the in-wheel motor T_L is defined as: $T_R : T_L = 1 : 4.7$. The key parameters of the DIW-PM motors are shown in Table II. And based on the moment of inertia and (42), the tuning friction damping coefficient of 0.4 is selected for motor #I, while 1.6 is selected for motor #II.

A. Left and Right In-Wheel Drive Mode

The LR in-wheel drive on the same side is selected as an integrated system, which is cooperative and controlled by the ELM-TA controller. In order to verify the effectiveness of algorithm synchronization, two conditions are simulated. Additionally, motor #I and motor #II represent the left and right in-wheel motors.

1) Variable Speed Condition: In Fig. 7, the ELM-TA control shows better performance in speed increase command, effectively enhancing dynamic response performance to 37.5% of motor #I and 27.2% of motor #II. Besides, the ELM-TA control can dynamically assign torque to achieve speed synchronization. Especially, when the mechatronic system increases a torque load of 29.2 N·m, the electromagnetic torque difference of ELM-TA control added to the left and right motors is 21.7 N·m and 7.7 N·m respectively, while the MSDTC control is 14.9 N·m and 13.8 N·m. Furthermore, the MSDTC control evenly assigns the total load and cannot effectively and quickly track commands for the left front wheel under straight operation conditions.

2) Muddy Road Condition: The experimental results in muddy road condition are shown in Fig. 8. Simultaneously, Fig. 8(b) and 8(d) respectively display the harmonic distortion analysis of the phase current, which are extracted from the zoomed sections of Fig. 8(a) and 8(c). During the sudden increase in load stage, under the MSDTC control, the vehicle

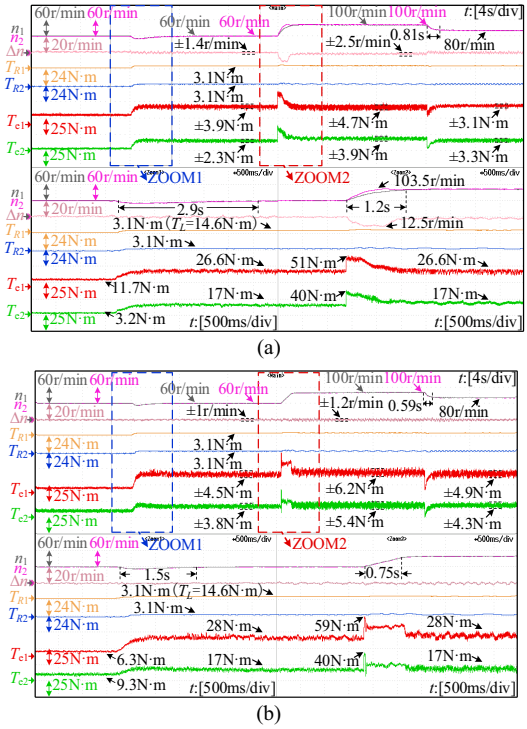

Fig. 7. Waveforms of variable speed experiment. (a) MSDTC control. (b) ELM-TA control.

deviates from the straight line while the right wheel motor exhibits significant oscillations. The maximum speed difference Δn observed between the left and right motors reaches 17 r/min, while the speed of the right in-wheel motor fluctuates around 4.5 r/min until convergence. This adjustment can take up to 13.3 s, resulting in a sluggish overall response performance.

Nonetheless, for the ELM-TA control, the left and right motors can effectively synchronize. During a substantial increase in load, a maximum speed difference of 2.6 r/min is observed. Compared with the MSDTC control, the adjustment time of the left and right motors under the ELM-TA control is reduced by 64.2% and 85.7%, respectively. According to Fig. 9(b) and 9(d), although the ELM-TA control increases torque pulsation, it effectively reduces the phase current harmonics of left and right motors to 12.29% and 16.32%.

B. Front and Rear In-Wheel Drive Mode

On the other hand, the FR in-wheel drive on the same side can also be selected as an integrated system, cooperative and controlled by one controller. And, motor #I and motor #II represent the front and rear in-wheel motors.

1) Variable Speed Condition: Fig. 9 illustrates the ability of both algorithms to accurately track the speed command n_{ref} during the front wheel loading and acceleration stages, while the ELM-TA control demonstrates superior performance, effectively improving 54.7% of dynamic response performance and 35.7% of speed synchronization performance. Additionally, the MSDTC control resulted in a maximum speed difference Δn of 11.9 r/min, causing oscillate and slip significantly, deviating from the given route. Nevertheless, although the ELM-TA control relinquishes

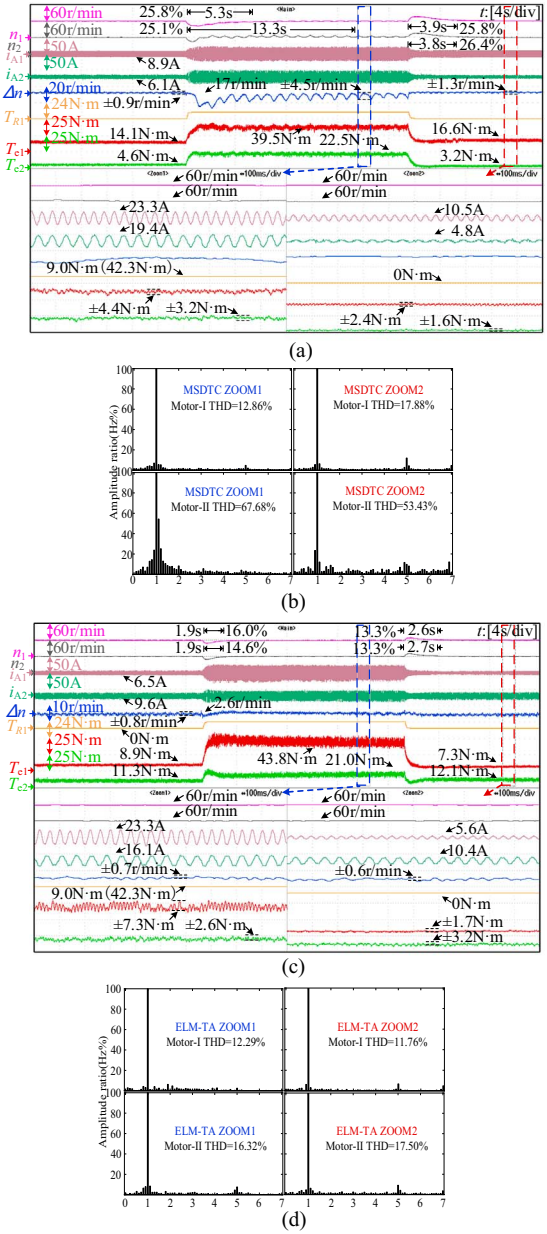

Fig. 8. Waveforms under the muddy road condition. (a) MSDTC control on muddy long road. (b) Current analysis of MSDTC. (c) ELM-TA control on muddy long road. (d) Current analysis of ELM-TA control.

torque ripple to a certain degree, it effectively apportioned torque to the rear wheels, diminished the maximum Δn by 83.2%, and guaranteed synchronization and stability.

2) Muddy Road Condition: In Fig. 10, the front and rear wheels are loaded with 22.1 N·m sequentially under muddy long road, and the front wheel are loaded and unloaded with 43.7 N·m, followed by the rear wheel being loaded and unloaded with 43.7 N·m. Fig. 10(b) and 10(d) show the harmonic analysis of a-phase current in the zoomed part.

It can be observed that the ELM-TA control strategy demonstrates a notable enhancement in load synchronization capability when the front wheel encounters a muddy road condition. The current of the rear motor effectively increases to 12 A, actively distributing the front wheel load, and improving the dynamic

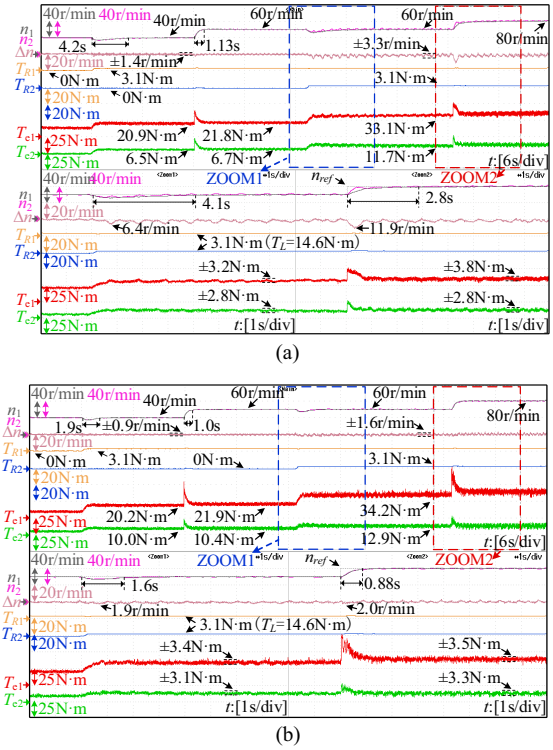

Fig. 9. Waveforms of variable speed experiments. (a) MSDTC control. (b) ELM-TA control.

synchronization ability under sudden external disturbances. Furthermore, during the rear wheel engages stage, the MSDTC control cannot effectively cooperative in torque assignment, which leads to severe vibration and slipping due to the unbalanced shaft torque of the flexible coupling. However, in order to alleviate burden on the rear wheel, ELM-TA control increases the front motor current to 25 A, effectively reducing the overshoot of the front and rear in-wheel motors by 64% and 34%, respectively. It also simultaneously reduces the THD of phase current to 9.39% and 15.82%.

Fig. 10(e) and 10(f) reveal a deficiency in the rear wheel load capacity, causing the torque balance between the front and rear wheels to collapse due to the limitations of torque assignment of MSDTC control. This imbalance results in yaw torque generation through mutual dragging, causing seriously slip and oscillate, and unable to effectively track driving instructions. The rear wheel oscillation duration can extend up to 8.4 s, emphasizing the critical need to avert wheel control loss by swift torque allocation. Consequently, the ELM-TA control mechanism serves to mitigate this issue by reducing the current flowing through the rear wheel, enhancing the electromagnetic torque allocated by the front wheel, reducing the rear wheel phase current to 13.3 A, and minimizing the distributed torque to 10.8 N·m. Besides, ELM-TA control effectively diminishes the overshoot of the front and rear motors by 43% and 33%, respectively, achieving fast synchronization and tracking.

C. Dynamic Performance Comparison

In order to more intuitively illustrate the effectiveness of the ELM-TA control system, the performance metrics are shown in

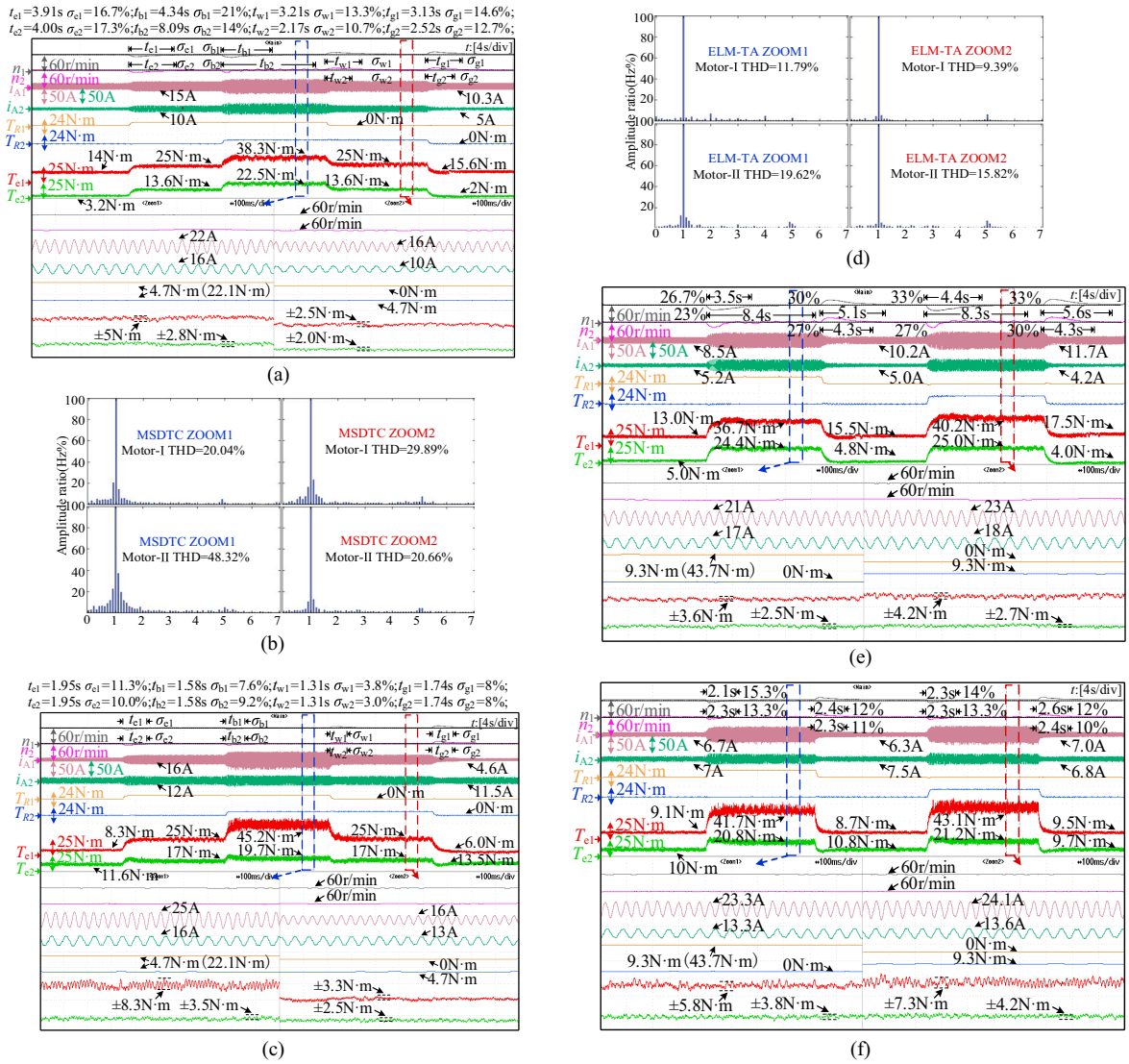

Fig. 10. Waveforms under muddy road conditions. (a) MSDTC control on muddy long road. (b) Current analysis of MSDTC control. (c) ELM-TA control on muddy long road. (d) Current analysis of ELM-TA control. (e) MSDTC on muddy short road. (f) ELM-TA control on muddy short road.

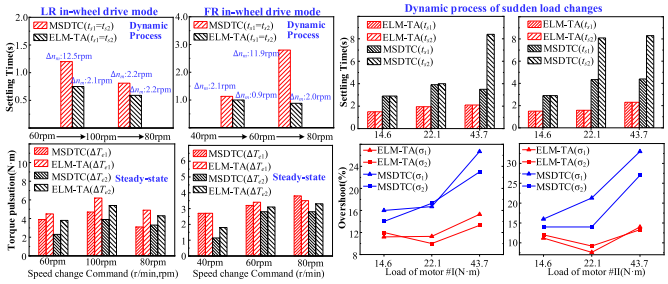

Fig. 11. Dynamic performance comparison.

Fig. 11 in conjunction with all the previous experimental plots, and a table of performance comparisons under high-load scenarios is shown in Table III.

As shown in Fig. 11, during the execution of a speed change command, Δnm denotes the maximum speed differential, while ΔT_{e1} and ΔT_{e2} represent the torque ripple of motor #I and motor #II under constant speed conditions, respectively. Additionally, the adjustment times are denoted, with t_{s1} and t_{s2} representing the adjustment durations for motor #I and motor #II, respectively. Furthermore, σ_1 and σ_2 signify the overshoot for each motor. It is noteworthy that the x-axis of the graphs illustrates the sudden increase in load values.

It can be seen that the ELM-TA control can respond to variable speed commands within 1 s, significantly enhancing the dynamic response performance of Motor #I by over 40.0% and Motor #II by more than 48.3%. This improvement substantially reduces speed differentials and enhances synchronization, ensuring stable vehicle operation under complex working conditions. Nevertheless, MSDTC requires a longer settling time, with a maximum speed difference of 12.5 rpm during variable speed scenarios. Furthermore, ELM-TA effectively reduces overshoots and oscillations during dynamic processes, enabling stable operation of the vehicle under high-load scenarios and variable commands.

Moreover, to further validate the dynamic response performance and robustness of the proposed algorithm, Fig. 12 simulates the DIW-PM system traversing a bumpy road surface. This

TABLE III
DYNAMIC PERFORMANCE COMPARISON IN HIGH LOAD

High-load Scenarios	FR Drive Mode				LR Drive Mode	
	Motor-I (43.7 N·m)		Motor-II (43.7 N·m)		Motor-I (42.3 N·m)	
	MSDTC	ELMTA	MSDTC	ELMTA	MSDTC	ELMTA
σ_1	26.7%	15.3%	33.0%	14.0%	25.8%	16.0%
σ_2	23.0%	13.3%	27.0%	13.3%	25.1%	14.6%
t_{s1} (s)	3.5	2.1	4.4	2.3	5.3	1.9
t_{s2} (s)	8.4	2.3	8.3	2.3	13.3	1.9
Oscillation	YES	NO	YES	NO	YES	NO
ΔT_e(±N·m)	3.6 (1) 2.5 (2)	5.8 (1) 3.8 (2)	4.2 (1) 2.7 (2)	7.3 (1) 4.2 (2)	4.4 (1) 3.2 (2)	7.3 (1) 2.6 (2)

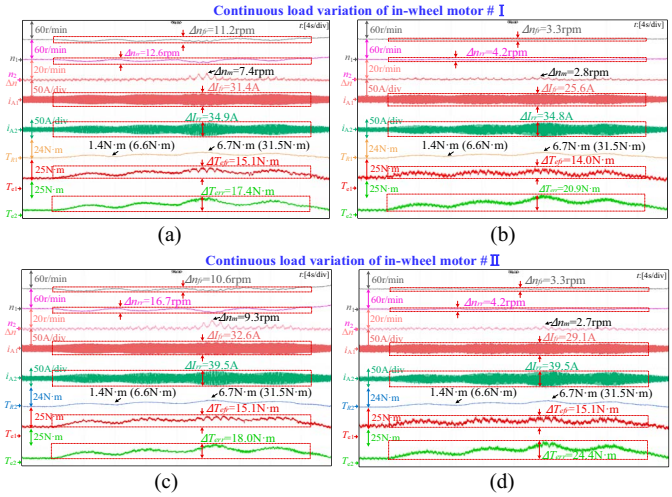

Fig. 12. Waveforms of bumpy road condition. (a) MSDTC control (motor #I load). (b) ELM-TA control (motor #I load). (c) MSDTC control (motor #II load). (d) ELM-TA control (motor #II load).

experiment illustrates the continuous variation in the loads of in-wheel motor #I load T_{R1} and in-wheel motor #II load T_{R2}, with both loads fluctuating continuously between 6.6 N·m and 31.5 N·m.

Compare with MSDTC, it can be observed that the maximum speed fluctuations of motor #I and motor #II are reduced by 70.6% and 66.7%, respectively, under ELM-TA control when subjected to continuous load variation in motor #I, with the speed difference maintained within 2.8 r/min. Additionally, torque fluctuations are minimized, and current fluctuations are reduced, enabling motor #II to share the load in real time, thereby enhancing synchronization. Under load variation in motor #II, the ELLM-TA system achieves a 68.9% and 74.9% reduction in speed fluctuations for motor #I and motor #II, respectively, while the maximum speed difference decreases by 70.9%. Despite increased loads, the speed remains stable at 60 r/min, preventing tire shake and yawing on challenging road conditions.

It can be noted that the ELM-TA control optimizes the system architecture by reducing the number of required controllers and actuators, effectively alleviating the computational burden on the VCU. The ELM-TA control can better cope with scenarios with significant load variations and higher dynamic performance requirements, such as off-road or muddy terrains.

V. CONCLUSION

In this article, an ELM-TA control with MVV modulation is proposed for DIW-PM motors drive system. The mechatronic system model of DIW-PM motors is deduced. Moreover, based on the DTC principle, the ELM-TA control system is presented and investigated. And then, a decoupling tuning method for interconnection and friction damping coefficients is designed to improve the robustness of the DD system.

Consequently, by the experimental setups with different in-wheel drive modes and road conditions, the ELM-TA control performance is demonstrated and discussed. The results show that, compared with the MSDTC, the proposed control method can improve resistance to external environmental interference by 57.2%, achieve a comprehensive balance between fast speed tracking, and smooth driving, with a significant improvement in dynamic response performance by 40.0%-80.5%. Furthermore, the ELM-TA control can achieve active torque assignment, with speed as a constraint, coordinate the load situation of each motor, and improve the system's load capacity by 49.4% while maintaining synchronization. The study provides a new research approach for achieving torque assignment control under high synchronization performance in the DD system where the number of MCUs are reduced and the responsiveness and robustness of the system is improved.

Furthermore, in the future, taking into account the energy consumption and the development requirements for intelligent driving in EVs, a deep coupling model of the multiple in-wheel PM motors will be constructed and the predictive control can be also introduced for the cooperative control of the DD system. This will serve to further enhance the robustness of the multiple in-wheel PM motors, reduce the computational load of the VCU, and improve the reliability of the system.

REFERENCES

[1] B. Guo and Y. Chen, "Robust adaptive fault-tolerant control of four-wheel independently actuated electric vehicles," *IEEE Trans. Ind. Informat.*, vol. 16, no. 5, pp. 2882–2894, May 2020.
[2] N. Guo et al., "A real-time nonlinear model predictive controller for yaw motion optimization of distributed drive electric vehicles," *IEEE Trans. Veh. Technol*, vol. 69, no. 5, pp. 4935–4946, May 2020.
[3] L. Xu et al., "Multiple-mode current control for a hybrid-excitation axial flux switching permanent magnet motor considering driving cycles," *IEEE Trans. Ind. Electron.*, vol. 71, no. 1, pp. 204–214, Jan. 2024.
[4] H. Zhou, F. Jia, H. Jing, Z. Liu, and L. Güvenç, "Coordinated longitudinal and lateral motion control for four wheel independent motor-drive electric vehicle," *IEEE Trans. Veh. Technol.*, vol. 67, no. 5, pp. 3782–3790, May 2018.
[5] Z. Liu et al., "A hierarchical anti-disturbance path tracking control scheme for autonomous vehicles under complex driving conditions," *IEEE Trans. Veh. Technol.*, vol. 70, no. 11, pp. 11244–11254, Nov. 2021.
[6] H. Zhou, Z. Liu, and X. Yang, "Motor torque fault diagnosis for four wheel independent motor-drive vehicle based on unscented Kalman filter," *IEEE Trans. Veh. Technol.*, vol. 67, no. 3, pp. 1969–1976, Mar. 2018.
[7] N. Guo, X. Zhang, Y. Zou, B. Lenzo, G. Du, and T. Zhang, "A supervisory control strategy of distributed drive electric vehicles for coordinating handling, lateral stability, and energy efficiency," *IEEE Trans. Transport. Electrific.*, vol. 7, no. 4, pp. 2488–2504, Dec. 2021.
[8] C. Liu, H. Liu, L. Han, W. Wang, and C. Guo, "Multi-level coordinated yaw stability control based on sliding mode predictive control for

distributed drive electric vehicles under extreme conditions," *IEEE Trans. Veh. Technol.*, vol. 72, no. 1, pp. 280–296, Jan. 2023.
[9] H. Peng et al., "Torque coordinated control of four in-wheel motor independent-drive vehicles with consideration of the safety and economy," *IEEE Trans. Veh. Technol.*, vol. 68, no. 10, pp. 9604–9618, Oct. 2019.
[10] Y. M. Mok, L. Zhai, C. Wang, X. Zhang, and Y. Hou, "A post impact stability control for four hub-motor independent-drive electric vehicles," *IEEE Trans. Veh. Technol.*, vol. 71, no. 2, pp. 1384–1396, Feb. 2022.
[11] T. Ghandriz, B. Jacobson, P. Nilsson, L. Laine, and N. Fröjd, "Computationally efficient nonlinear one- and two-track models for multi-trailer road vehicles," *IEEE Access*, vol. 8, pp. 203854–203875, 2020.
[12] Y. Xiao, X. Zhang, X. Xu, X. Liu, and J. Liu, "Deep neural networks with Koopman operators for modeling and control of autonomous vehicles," *IEEE Trans. Intell. Veh.*, vol. 8, no. 1, pp. 135–146, Jan. 2023.
[13] Z. Liu et al., "A passivity-based control of Euler–Lagrange model for suppressing voltage low-frequency oscillation in high-speed railway," *IEEE Trans. Ind. Inform.*, vol. 15, no. 10, pp. 5551–5560, Oct. 2019.
[14] F. Wang and Y. Chen, "Vehicle rollover propensity detection based on a mass-center-position metric: A continuous and completed method," *IEEE Trans. Veh. Technol.*, vol. 68, no. 9, pp. 8652–8662, Sep. 2019.
[15] H. Chen, J. Zhang, and C. Lv, "RHONN modelling-enabled nonlinear predictive control for lateral dynamics stabilization of an in-wheel motor driven vehicle," *IEEE Trans. Veh. Technol.*, vol. 71, no. 8, pp. 8296–8308, Aug. 2022.
[16] F. Gao, Y. Han, S. Eben Li, S. Xu, and D. Dang, "Accurate pseudospectral optimization of nonlinear model predictive control for high-performance motion planning," *IEEE Trans. Intell. Veh.*, vol. 8, no. 2, pp. 1034–1045, Feb. 2023.
[17] D. Xiao, X. Li, and K. He, "Power balance of starting process for pipe belt conveyor based on master-slave control," *IEEE Access*, vol. 6, pp. 16924–16931, 2018.
[18] X. Su, "Master–Slave control for active suspension systems with hydraulic actuator dynamics," *IEEE Access*, vol. 5, pp. 3612–3621, 2017.
[19] H. Hwang, H. Choi, and K. Nam, "Practical synchronous steering angle control of a dual-motor driving steer-by-wire system," *IEEE Access*, vol. 7, pp. 133100–133110, 2019.
[20] J. Xie, X. Xu, F. Wang, Z. Liu, and L. Chen, "Coordination control strategy for human-machine cooperative steering of intelligent vehicles: a reinforcement learning approach," *IEEE Trans. Intell. Transp. Syst.*, vol. 23, no. 11, pp. 21163–21177, Nov. 2022.
[21] X. Zeng, Y. Wang, D. Song, L. Zhu, G. Tian, and Z. Li, "Coordinated control algorithm of a dual motor for an electric variable transmission hybrid system," *IEEE Access*, vol. 6, pp. 35669–35682, 2018.
[22] H. Deng, Y. Zhao, A.-T. Nguyen, and C. Huang, "Fault-Tolerant predictive control with deep-reinforcement-learning-based torque distribution for four in-wheel motor drive electric vehicles," *IEEE/ASME Trans. Mechatron.*, vol. 28, no. 2, pp. 668–680, Apr. 2023.
[23] J. Zhang, W. Sun, and H. Du, "Integrated motion control scheme for four-wheel-independent vehicles considering critical conditions," *IEEE Trans. Veh. Technol.*, vol. 68, no. 8, pp. 7488–7497, Aug. 2019.
[24] L. Zhang et al., "Space decoupling sensorless control of five-phase flux-intensifying PM motor based on AFCCF-SMO considering flux-weakening operation," *IEEE Trans. Ind. Electron.*, early access, Jan. 1, 2025, doi: 10.1109/TIE.2024.3519592.
[25] R. Ortega et al., *Passivity Based Control of Euler Lagrange Systems: mechanical, Electrical and Electromechanical Applications*. New York, NY, USA: Springer Sci. & BusinessMedia, 2013.
[26] B. Brogliato, R. Lozano, B. Maschke, and O. Egeland, "Dissipative systems analysis and control," *Theory Appl.*, vol. 2, 2007.
[27] Y. Wang et al., "Dissipative Hamiltonian realization and energy-based L_2-disturbance attenuation control of multimachine power systems," *IEEE Trans. Automat. Control*, vol. 48, no. 8, pp. 1428–1433, Aug. 2003.
[28] F. Niu et al., "Comparative evaluation of direct torque control strategies for permanent magnet synchronous machines," *IEEE Trans. Power Electron.*, vol. 31, no. 2, pp. 1408–1424, Feb. 2016.
[29] Y. Zhang and J. Zhu, "Direct torque control of permanent magnet synchronous motor with reduced torque ripple and commutation frequency," *IEEE Trans. Power Electron.*, vol. 26, no. 1, pp. 235–248, Jan. 2011.
[30] Z. Wang, X. Zhu, L. Xu, W.-H. Chen, Q. Liu, and L. Quan, "Multi-voltage-vector-modulation-based integrated direct torque control of dual in-wheel PM motors for distributed drive electric vehicles," *IEEE Trans. Ind. Electron.*, early access, Jan. 1, 2024, doi: 10.1109/TIE.2024.3482000000000000000000.

Zhaoheng Wang received the B.Sc. degree in electrical engineering and automation from the School of Electrical Engineering, Southeast University, Nanjing, China, in 2022. He is currently working toward the M.Sc. degree in electrical engineering with Jiangsu University, Zhenjiang, China.

His research interests include control of permanent magnet synchronous motor control and the cooperative control of multiple motors.

Lei Xu (Member, IEEE) received the B.Sc. degree in electrical engineering and automation from Yancheng Institute of Technology, Yancheng, China, in 2010, the M.Sc. degree from Jiangsu University, Zhenjiang, China, in 2013, and the Ph.D. degree from the Southeast University, Nanjing, China, in 2017, both in electrical engineering.

Currently, he is an Associate Professor with the School of Electrical and Information Engineering, Jiangsu University. His research interests include the high-performance permanent magnet motors, the development of advanced motor control strategies, and their applications in aerospace, automotive engineering, renewable energy generation system, and intelligent manufacturing equipment system.

Xiaoyong Zhu (Member, IEEE) received the B.Sc. and M.Sc. degrees from Jiangsu University, Zhenjiang, China, in 1997 and 2002, respectively, and the Ph.D. degree from the School of Electrical Engineering, Southeast University, Nanjing, China, in 2008, all in electrical engineering. During the period of doctoral study, his subject is electrical engineering, which mainly focuses on the design, analysis and control of the type of hybrid-excited permanent magnet machine.

Since 1999, he has been with Jiangsu University, where he is currently a Professor with the School of Electrical Information Engineering. From 2007 to 2008, he was a Research Assistant with the Department of Electrical and Electronic Engineering, University of Hong Kong, Hong Kong. From 2012 to 2013, he was a Visiting Professor with the Department of Energy-Funded Graduate Automotive Technology Education Center for Electric Drive Transportation, University of Michigan, Dearborn, MI, USA. He has authored or co-authored more than 70 referred technical papers, and holds 12 patents in his research field, which include design and drive control of electric machines with wide-speed range, less rare-earth permanent magnet motor, and multiport permanent magnet motor.

Li Quan received the B.Sc. degree in electrical engineering from Hefei University of Technology, Hefei, China, in 1985, the M.Sc. degree in motors and electrical specialty from the Southeast University, Nanjing, China, in 1991, and the Ph.D. degree in power electronics and power transmission from Nanjing University of Aeronautics and Astronautics, Nanjing, in 2007.

Since 1998, he has been with Jiangsu University, Zhenjiang, China, where he is currently a Professor with the School of Electrical and Information Engineering. He has authored or co-authored more than 100 technical papers, one textbook, and holds three patents in these areas. His teaching and research interests include high performance permanent magnet motor for electric vehicles (EVs), double rotor permanent magnet motor for hybrid electric vehicles (HEVs) and motor drives control.

Wen-Hua Chen (Fellow, IEEE) received the M.Sc. and Ph.D. degrees in control engineering from the Department of Automatic Control, Northeastern University, Shenyang, China, in 1989 and 1991, respectively.

From 1991 to 1996, he was a Lecturer with the Department of Automatic Control, Nanjing University of Aeronautics and Astronautics, Nanjing, China. From 1997 to 2000, he held a research position and then a lectureship in control engineering with the Centre for Systems and Control, University of Glasgow, Glasgow, U.K. Currently, he is a Professor in autonomous vehicles with the Department of Aeronautical and Automotive Engineering, Loughborough University, Loughborough, U.K. He has authored or co-authored three books and 350 papers in journals and conferences. His research interests include the development of advanced control strategies and their applications in aerospace and automotive engineering, particularly in unmanned electric aircraft and vehicles.

Dr. Chen was a fellow of the Institution of Mechanical Engineers (FIMechE) in 2015 and Institution of Engineering and Technology (IET) in 2013. He was the recipient of the EPSRC Established Career Fellowship Award of U.K.

Lizhang Xu received the B.Eng., M.S., and Ph.D. degrees in agricultural engineering from Jiangsu University, Zhenjiang, China, in 2000, 2003, and 2009, respectively.

From 2005 to 2011, he was a Research Assistant with the College of Agricultural Engineering, Jiangsu University. From 2011 to 2015, he was an Associate Researcher with the College of Agricultural Engineering. Since 2015, he has been a Researcher with the College of Agricultural Engineering. His research interests include environmental information perception and precision operation of harvesting machinery, unmanned harvesting machinery and artificial intelligence systems, design theory, and structural innovation of multicrop harvesting machinery.

Dr. Xu was a recipient of First Prize for Science and Technology Progress of the Ministry of Education, Second Prize of National Technological Invention Award, and 16th China Youth Science and Technology Award.

Shihong Ding (Senior Member, IEEE) was born in Anhui, China, in 1983. He received the B.E. degree in mathematics from Anhui Normal University, Wuhu, China, in 2004, and the M.S. and Ph.D. degrees in automatic control from the Southeast University, Nanjing, China, in 2007 and 2010, respectively.

During the graduate studies, he visited The University of Texas at San Antonio, San Antonio, TX, USA, from 2008 to 2009. After graduation, he held a Research Fellowship with the University of Western Sydney, Parramatta, NSW, Australia, for one year. He also visited Yeungnam University, Gyeongsan, South Korea in 2018, and RMIT University, Melbourne, VIC, Australia, from 2019 to 2020, respectively. Since 2010, he has been with the School of Electrical and Information Engineering, Jiangsu University, Zhenjiang, China, where he is currently a Full Professor. His research interests include sliding-mode control and motion control.

Dr. Ding is currently a Subject Editor for Nonlinear Dynamics and an Associate Editor for *International Journal of Adaptive Control and Signal Processing*.